Ceramics International xxx (xxxx) xxx

Contents lists available at ScienceDirect

Ceramics International

journal homepage: www.elsevier.com/locate/ceramint

Experimental, analytical, and numerical quantification of the Marangoni effect in static refractory finger test

Sandra Vollmann [a,*], Jerónimo Guarco [b], Burhanuddin [a]

[a] Montanuniversität Leoben, Chair of Ceramics, Peter-Tunner-Strasse 5, 8700, Leoben, Austria
[b] K1-MET GmbH, Stahlstraße 14, 4020, Linz, Austria

ARTICLE INFO

Handling Editor: Dr P. Vincenzini

Keywords:
C. Corrosion
D. Al_2O_3MgO
E. Refractories

ABSTRACT

This study investigated the local corrosion of alumina and magnesia refractory in $CaO–Al_2O_3–SiO_2–MgO$ slag due to the Marangoni effect, which is a key factor for localized wear in different industrial processes, using experimental, analytical, and numerical approaches. The objective is to explore the Marangoni effect using computational fluid dynamics simulation aiming to provide insights into the dominant slag flow patterns influencing refractory corrosion and to determine whether the observed corrosion groove can be attributed solely to the Marangoni effect. Static finger tests were conducted at temperatures of 1500 and 1550 °C employing a continuous wear testing device. A two-dimensional axisymmetrical section model of the test assembly was created, incorporating concentration-dependent surface tension gradients and surface tension forces to replicate the Marangoni flow. As the surface-tension simulation required time steps in the order of 10^{-5} s, modeling up to the experimental time scale cannot be realized. Consequently, the simulation outcomes were extrapolated to anticipate the groove radii of the experimental corrosion steps. Corrosion rates were derived from measurements and analytical methodologies. Established analytical equations for corrosion under surface-tension-flows were adapted to enhance the accuracy of corrosion rate estimation. However, the analytical considerations yielded poor estimates. Meanwhile, the employed simulation model successfully generated plausible predictions of the Marangoni flow. Drawing from the extrapolated simulation outcomes, the projected groove radii exhibited a close correspondence to the measured values, demonstrating a relative error of approximately 3 %, 11 %, and 15 % for the magnesia system at 1500 °C and alumina systems at 1500 and 1550 °C, respectively. Taking into account the uncertainties inherent in the methodological approach, the disparities in the alumina values suggest the involvement of mechanisms beyond the Marangoni effect in the localized wear. Consequently, this study effectively clarifies the impact of the Marangoni effect on the local wear of the examined material systems.

1. Introduction

The lifespan of refractory linings is constrained by localized wear occurring at phase boundaries, as documented in Refs. [1,2]. The presence of surface tension gradients along the fluid interface induces fluid flow, consequently expediting wear in proximity to the triple line involving refractory/slag/atmosphere or refractory/melt/slag. In the context of refractory applications, surface-tension gradients are ascribed to temperature gradients or localized changes in chemical composition during the dissolution of refractory oxides in the slag. In instances involving carbon-bearing refractories, the oxygen concentration in the steel melt is influenced by the reducing action of solid carbon within the refractory.

The Marangoni effect distinguishes itself as a pivotal factor influencing localized wear in various industrial processes, including yet not limited to glass furnaces, as well as metallurgical operations involving steel ladles or submerged entry nozzles [3–6]. Exploration of the Marangoni effect in diverse material systems has been undertaken [7–18]. Hrma [17] formulated an analytical equation for the corrosion rate by postulating a velocity distribution of the capillary convection within the creeping flow and employing polynomial concentration profiles. Drawing upon analytical examinations of mass transfer within the slag film, Pötschke and Brüggmann [19] proposed an equation for the mass transfer coefficient attributed to the Marangoni flow. This equation

Abbreviations: CASM, $CaO–Al_2O_3–SiO_2–MgO$; CFD, computational fluid dynamics; CWTD, continuous wear-testing device; VOF, volume of fluid.

* Corresponding author.
E-mail address: sandra.vollmann@unileoben.ac.at (S. Vollmann).

https://doi.org/10.1016/j.ceramint.2024.06.215
Received 30 January 2024; Received in revised form 12 June 2024; Accepted 15 June 2024
Available online 28 June 2024

facilitated the evaluation of corrosive mass transfer from the material system from measured corrosion groove height and properties of the material system. Fagerlund et al. [20] established a condition for achieving a stable Marangoni flow below the critical Reynolds number by deducing from dynamic finger tests, while accounting for the influences of wear. Burhanuddin et al. [21] identified the critical Reynolds number for alumina in a silicate melt of $CaO–Al_2O_3–SiO_2–MgO$ (CASM) with 0.65 wt% CaO/SiO_2 at 1550 °C using the experimental results obtained from a finger test device with high-accuracy measurement of the sample dimensions at the test temperature via laser scanning.

Beyond experimental inquiries, understanding the mechanisms underlying wear can be advanced through modeling and simulation. Computational fluid dynamics (CFD) unveils the dominant flow patterns that dictate species mass transfer and conditions conducive to corrosive wear. Erosive wear, induced by fluid flow, is attributed to wall shear stresses. Nevertheless, it is noteworthy that surface tension simulations predominantly center around droplets and their dynamics in terms of formation and spreading [22–27]. In the field of metallurgy, surface tension simulations are widely used to model the Marangoni flow of the molten pool during laser melting [28,29] and welding [30]. Ou et al. [31] utilized simulations and experiments to explore the solid dissolution of liquid metals in ice/water and ethanol/water systems, employing them as analogous physical models. Buoyancy and Marangoni convection played a significant role in influencing heat and mass transfer when forced convection did not dominate the flow field. Concurrently, additional researchers developed computational methods [32–36]. Nevertheless, achieving stable and accurate simulation of the Marangoni effect poses challenges due to the intricacies of modeling. This includes the representation of variable surface tension, which demands small time steps and adequate spatial discretization [37–42]. Moreover, the material systems under investigation in the current study exhibit large Schmidt numbers, necessitating a high spatial resolution of the computational domain to ensure an accurate solution of the species transport equation. In a previous work [43], CFD was applied to quantify the Marangoni convection with respect to refractory corrosion. The simulation outcomes of the dynamic finger test conducted on silica in fayalitic slag align with the experimental findings reported by Fagerlund et al. [20]. Moreover, the notable impact of the Marangoni effect on refractory wear below a determined critical Reynolds number was identified. In this case, the mass transfer equations reported in literature [19] yielded poor estimates. Few researchers further reported the CFD simulation of the finger test. Guarco et al. [44] deduced a Sherwood correlation for the corrosion during the finger test by simulations considering the actual shape of the corroded samples. Erosive wear resulting from shear stresses induced by slag flow was examined by employing an alternative CFD model for the finger test. This model took into account the changing sample geometry, enabling the inverse determination of erosion parameters [45]. Wang et al. [46] presented a three-dimensional solid–fluid coupled model of a finger-test setup to predict the overall wear rate using a kinetic degradation model that combined the flow-induced erosion and chemically induced corrosion. The erosive wear rate was calculated by computing the wall shear stresses and correlating them with the refractory mass loss using a power law. Simultaneously, a modified Arrhenius approach was utilized to determine the corrosive wear. Coefficients for erosion and corrosion rates were derived from experiments and adjusted based on industrial measurements, forming the mathematical expression for the overall wear rate implemented in the CFD simulation. Despite considering wetting behavior, a constant surface tension was employed, leading to the exclusion of Marangoni convection. A similar kinetic degradation model was also applied to refractory linings, as observed in the context of steel ladles [47]. The examination of the effects of flow phenomena on corrosive mass transfer at elevated temperatures can only be accomplished through simulation. Although CFD finger test simulations have been used to examine dissolution under forced convection [44] and erosion [45], the impact of Marangoni flow on corrosive mass transfer of magnesia and alumina has not been investigated. Although Wang et al. [46] have mentioned the Marangoni effect, their model does not account for the effect. In contrast, the current methodology takes into consideration surface tension gradients and surface tension forces, thereby incorporating Marangoni convection. The impact of Marangoni convection on species concentration for corrosive mass transfer is governed by the advection-diffusion equation. Consequently, the convection driven by surface tension gradients, representing the physical force propelling local corrosion phenomena, is explicitly addressed. Such consideration is essential for elucidating the local corrosion mechanisms and the pivotal factors influencing them.

In this study, CFD was applied to investigate the flow field induced by surface-tension gradients, affecting the diffusion-controlled corrosive mass flux for two material systems of magnesia and alumina in CASM slag with 0.65 wt% CaO/SiO_2 at 1500 and 1550 °C. The investigation exclusively addressed static cases, omitting sample rotation, and prioritized scenarios where local corrosion prevailed. Emphasis was placed on delineating the flow field solely induced by the Marangoni effect. The precise measurement of sample dimensions using the laser in the finger-test device enabled refined adjustments to analytical considerations. The study pursued a threefold objective: simulating the Marangoni flow, quantifying its impact on corrosive mass transfer, and determining if groove formation through local corrosion could be exclusively ascribed to Marangoni convection.

2. Materials and methods

2.1. Material systems and properties

Static corrosion tests at 1500 and 1550 °C were performed on magnesia fine ceramics with 99.6 wt% MgO and a bulk density of 3400 kg/m^3 (Surtec Research Europe GmbH, Düsseldorf, Germany) and alumina fine ceramics with 99.7 wt% Al_2O_3 and a bulk density of 3870 kg/m^3 (Ants Ceramics Private Limited, India) in the CASM slag with 32.42 wt% CaO, 11.16 wt% Al_2O_3, 49.56 wt% SiO_2 and 6.86 wt% MgO. The CASM slag was compounded from decarburized $CaCO_3$, alumina powder, quartz powder, and MgO powder (S3 Handel und Dienstleistungen UG, Germany). The slag viscosities (μ) and densities (ρ), binary diffusion coefficients for magnesia (D_M) and alumina (D_A), saturation limits in weight percent ($w_{s,M}$ and $w_{s,A}$, respectively), and

Table 1
Material properties.

Test temperature		1500 °C	1550 °C
Viscosity μ	/Pa·s	0.7282	0.5295
Density ρ	/kg/m^3	2587	2579
Diffusion coefficient of alumina D_A	/m^2/s	4.25×10^{-11}	7.44×10^{-11}
Diffusion coefficient of magnesia D_M	/m^2/s	2.57×10^{-10}	
Saturation limit of alumina $w_{s,A}$	/1	0.4096	0.4464
Saturation limit of magnesia $w_{s,M}$	/1	0.2749	
Surface tension of initial slag σ_0	/N/m	0.4303	0.4207
Surface tension of alumina saturated slag $\sigma_{s,A}$	/N/m	0.5087	0.5093
Surface tension of magnesia saturated slag $\sigma_{s,M}$	/N/m	0.4871	

surface tension of the initial (σ_0) and magnesia- and alumina-saturated slag ($\sigma_{s,M}$ and $\sigma_{s,A}$, respectively) for the test temperatures are listed in Table 1. The viscosities and saturation limits were calculated by the thermochemical software FactSage 7.3 (CRCT, Montreal, QC, Canada), and the density was determined from the slag composition according to Xin et al. [48]. The effective binary diffusion coefficients were derived from dissolution studies conducted using confocal laser scanning microscopy [49,50], corresponding to the diffusion coefficients derived from the finger-test measurements using a continuous wear-testing device (CWTD) [51–53]. The correlation between surface tension and slag composition for magnesia and alumina was determined along the dissolution path, employing the model established by Xin et al. [54]. Following this, equations describing the relationship of the mass fraction of the dissolving species were formulated, as represented in Eqs. (1)–(3). Notably, surface tension exhibited an increase with the progression of dissolution in both investigated systems, corresponding to the accumulation of magnesia and alumina.

$$\sigma_{M,1500^\circ C} = 1.6204 \cdot w_M{}^2 - 0.2671 \cdot w_M + 0.4409 \quad /N/m, \tag{1}$$

$$\sigma_{A,1500^\circ C} = 0.2631 \cdot w_A + 0.4009 \quad /N/m, \tag{2}$$

$$\sigma_{A,1550^\circ C} = 0.2646 \cdot w_A + 0.3912 \quad /N/m. \tag{3}$$

2.2. Experiments

A state-of-the-art finger test set-up [55] was used to perform the static finger tests of the refractory/slag systems under the isothermal conditions at 1500 (magnesia and alumina) and 1550 °C (alumina). Cylindrical samples, having a radius of 10 mm and a length of 110 mm, were immersed in a slag bath at a height of approximately 65 mm, maintaining a bottom clearance of around 20 mm. Fig. 1 illustrates a picture of the interior of the furnace chamber of the CWTD used in the study. Upon reaching the designated test temperature, the laser

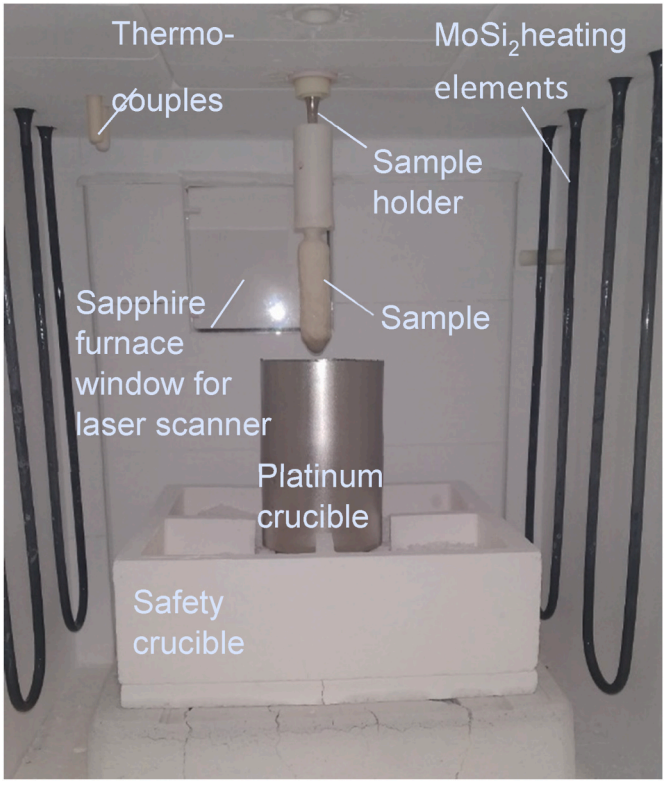

Fig. 1. Photograph of the furnace chamber in the continuous wear-testing device with a worn sample in the upper position.

systematically scans the sample surface, completing a full rotation around its axis to capture the entire surface through the sapphire furnace window. Subsequently, the cylindrical sample is immersed into a liquified slag bath within a platinum crucible. Following a specific immersion period, the sample is raised to an upper position to eliminate excess slag. Subsequently, the laser system scans the corroded sample surface. This cycle of immersion and measurement is iteratively executed for multiple corrosion steps within a single experiment. The laser measurement data undergo postprocessing, involving the averaging of circumferential values, resulting in a singular wear profile for each step.

2.3. Analytical investigation

Pötschke and Brüggmann [19] presented an equation for the mass transfer coefficient in a corrosion groove due to the Marangoni flow for refractory/slag systems based on the work of Levich (1962) for a mass transfer driven by a thermally induced surface tension gradient within a flat pan. Eq. (4) is employed to calculate the mass transfer coefficient β_1 (in m/s), following the methodology outlined by Pötschke (2012):

$$\beta_1 = \left(\frac{D \cdot d \cdot \Delta\sigma}{2\pi \cdot s^2 \cdot \mu}\right)^{1/2} \cdot \left(\frac{\rho \cdot D}{\mu}\right)^{1/6}, \tag{4}$$

where D is the diffusion coefficient in m^2/s, d is the thickness of the slag film ascending the refractory wall in m, $\Delta\sigma$ is the difference in the initial surface tension of the slag and that of the saturated state of the dissolving species in N/m, and s is the length of the corrosion groove in m, which is assumed to mark a half circle and is calculated from the measured groove height by Eq. (5):

$$s = 0.5 \cdot \pi \cdot h, \tag{5}$$

The determination of the slag film thickness involves the equilibrium between gravity and surface tension of a liquid wetting a vertical flat plate at a specific wetting angle (θ) using Eq. (6):

$$d = 2 \cdot \sigma \cdot \cos\theta / (\rho \cdot g \cdot h), \tag{6}$$

where g is the gravitational acceleration.

The measurement system used in this work accurately determined the geometry of the groove in terms of the x- and y-coordinates of the sample surface. Hence, the groove length can be ascertained through Eq. (7), based on the difference in the coordinates Δx and Δy of sequential data points within the groove:

$$s' = \sum_a^b \sqrt{\Delta x^2 + \Delta y^2}, \tag{7}$$

In determining the slag film thickness, an axisymmetric geometry of the slag film was taken into account, as expressed in Eq. (8):

$$d' = -r + \sqrt{\frac{\rho \cdot g \cdot h \cdot r^2 + 2 \cdot r \cdot \sigma \cdot \cos(\theta)}{\rho \cdot g \cdot h}}, \tag{8}$$

where r is the radius of the initial cylindrical refractory sample (0.01 m). Consequently, β_1 can be recalculated, denoted as β_2, using more accurate parameters of s' and d'.

The total mass transfer coefficient, incorporating the advection at the refractory/slag interface, is defined as:

$$\beta_{i,tot} = \chi \cdot \frac{1}{1 - w_s} \cdot \beta_i, \tag{9}$$

where index i is equal to 1 or 2, the correction factor χ accounts for the effect of interface advection on the fluid dynamics (Eq. (10)), B is the dimensionless concentration difference, w_0 is the initial mass fraction, and w_s is the mass fraction of dissolving species at the saturation limit (Eq. (11)). The factor $1/(1 - w_s)$ in Eq. (9) accounts for the convective

part of the dissolution mass flux density.

$$\chi \approx \frac{1}{1+0.566 \cdot B}, \tag{10}$$

$$B = \frac{w_s - w_0}{1 - w_s}, \tag{11}$$

From a flux balance at the refractory/slag interface, a corrosion rate v_i can be determined:

$$v_i = \frac{\rho}{\rho_r} \beta_{i,tot} \cdot \Delta w, \tag{12}$$

where ρ_r is the density of the dissolved refractory component. Hrma [17] considered the solid dissolution governed by free surface convection and defined a corrosion rate v_{Hrma} presupposing the small changes in the solute volume fraction C, given by Eq. (13):

$$v_{Hrma} = K \cdot \Delta C \cdot \left(\frac{D^2 \cdot \Delta^* \sigma \cdot g \cdot \rho}{\mu} \right)^{1/3}, \tag{13}$$

where surface tension is assumed to be linearly dependent on C, ΔC is the difference between the saturated and initial volume fractions of the dissolving species, D is the diffusion coefficient, and $\Delta^* \sigma$ is the relative surface tension difference defined by Eq. (14):

$$\Delta^* \sigma = \begin{cases} \dfrac{\Delta \sigma}{\sigma_{bulk}} & \text{for small } \Delta\sigma \\ 2 \cdot \left(1 + \dfrac{\sigma_{bulk}}{\Delta \sigma} \ln \dfrac{\sigma_{sat}}{\sigma_{bulk}} \right) & \text{for large } \Delta\sigma \end{cases}, \tag{14}$$

Different concentration profiles approximated by the polynomial functions within the liquid film were assumed, resulting in different factors K in the range of 0.2–0.4.

2.4. Simulation

Refractory corrosion is considered as a diffusion-controlled process of species mass transport of the dissolving refractory component into the slag. Here, the concept of effective binary diffusivity is applied, where the dissolving refractory component represents one species and all other slag components are grouped into a second species, namely the residual species. Thus, the slag phase is represented by a mixture of two species – the dissolving and the residual species. This necessitates a constant slag density. A boundary condition for one species only is required: the saturation limit of dissolving species in the slag at the specified temperature is defined at the refractory wall boundary. Following this, the dissolution mass flux density will be proportional to the diffusive mass flux of the dissolving species. The latter is given by Fick's 1st law of diffusion stating a proportionality to the species gradient at the refractory/slag interface. To obtain the species concentration field and the interface gradients the advection-diffusion equation needs to be solved which represents the additional scalar species transport equation in the model. The calculated species gradients allow for determination of the diffusive flux density. Beside the diffusive flux a convective flux contributes to the total dissolution flux. This convective flux results from the impermeability of the refractory to the residual species as stated by the Stefan condition. Since this convective flux is not considered in the model an additional correction factor needs to be introduced defined by Eq. (10). Lastly, the total dissolution mass flux results from affecting the diffusive flux by the correction factor and the additional factor $1/(1 - w_s)$ which accounts for the convective part.

Marangoni flow manifests at a free surface due to surface tension gradients induced by temperature and/or species variations. Thus, the prerequisites for conducting CFD simulations of Marangoni flow encompass the representation of both liquid and gas phases, their interface, surface tension linked to temperature and/or species mass fraction, and the pertinent energy and/or species transport equations. In this analysis, surface tension is regarded as a function solely dependent on species concentration, applicable only under isothermal conditions. The energy equation is omitted from the solution, and material properties are assumed constant at a high temperature. A user-defined function is incorporated to accommodate the concentration-dependent nature of surface tension. All material properties are detailed in Section 2.1.

Material systems with large Schmidt numbers, under investigation, necessitate a heightened mesh resolution within the simulation domain to accurately portray species transport. A diffusion coefficient in the order of 10^{-11} m^2/s and a typical mass transfer coefficient β in the order of 10^{-7} m/s based on the analytical considerations according to Pötschke [19] yields the thickness of the species boundary layer, which is defined as the ratio of D/β in the order of 10^{-4} m. Following the recommendation for the accurate solution of the species transport equation [37], a minimum of 10 cells should lay within this layer, yielding an estimated rectangular cell size in the order of 10^{-5} m in direction of species transport.

For every phenomenon incorporated in the simulation, an appropriate time step size was determined for the explicit calculation of the governing equations. The selected minimum time step sizes are designed to ensure a stable computation [38]. Denner et al. [39] exhibited time-step constraints in the volume-of-fluid (VOF) surface-tension simulation, utilizing implicit treatment for governing equations, aligning with observations in multiple studies encountering time-step limitations for implicit calculations. In their investigation, time-step sizes beyond a specified capillary time constraint were deemed suitable for two scenarios. The extent to which the time step could surpass the capillary time-step constraint was contingent on fluid densities, viscosities, and specific cases [40]. As a result, time-step constraints for the explicit method were computed to serve as a guideline. Table 2 lists a summary of the estimated time-step sizes for alumina in the CASM slag at 1550 °C and a characteristic mesh dimension h of 5×10^{-5} m. Accordingly, a time step of 6×10^{-6} s was recommended. Adaptive time advancement was used for all simulations with an initial time step size of 1×10^{-7} s and the maximum time step size of 5×10^{-5} s; the bounded 2nd order transient formulation was applied.

Only a segment of the finger test assembly was depicted in the two-dimensional axisymmetric model, as illustrated in Fig. 2, to achieve the requirements while ensuring the manageable computation time. The adequacy of the modeling effects in the vicinity of the triple point refractory/slag/atmosphere was verified and will be discussed in Section 3.3.1. The modeled domain has a height of 30 mm and spans radially from 10.0 mm to 32.5 mm. The quadratic cells possess dimensions of 10^{-4} m; ensuring finer resolution along the refractory/slag boundary and the initial slag/atmosphere interface, as well as within a half-circle around the initial triple point, the quadratic cell dimensions are 5×10^{-5} m. In the transition region from the coarse to the refined mesh quad- and triangular cells are placed. Achieving an accurate solution for species transport at the domain boundary involved representing refractory wall inflation layers, consisting of 10 cell layers with the smallest dimension of 2.6×10^{-6} m applied normally to the boundary. A

Table 2
Time-step size estimation for stable calculation.

Phenomenon		Ref.	Time-step size
Variable surface tension	$\Delta t_{\sigma\ Brackbill} = \sqrt{(\rho_a + \rho_b) \cdot h^3 / 4\pi\sigma}$/s	[42]	7.82×10^{-6}
Variable surface tension	$\Delta t_{\sigma Denner} = \sqrt{(\rho_a + \rho_b) \cdot h^3 / 2\pi\sigma}$/s	[40]	1.11×10^{-5}
Gravity	$\Delta t_g = \sqrt{h/9.81}$/s	[38]	2.26×10^{-3}
Viscous flow	$\Delta t_\mu = \sqrt{\rho \cdot h^2/(2\mu)}$/s	[38]	6.09×10^{-6}
Diffusion	$\Delta t_D = \sqrt{\rho \cdot h^2/(2D)}$/s	[38]	4.33×10^{4}

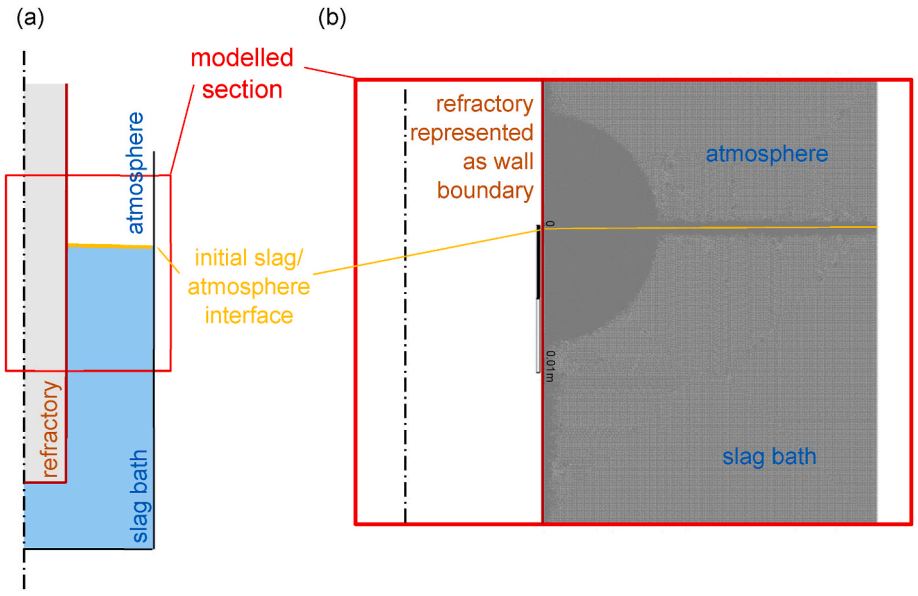

Fig. 2. Schematic of the symmetric half of the finger test (a) and numerical mesh of the simulation model, including the refined slag/refractory and slag/atmosphere interfaces (b).

total of 103 740 cells were obtained for the mesh.

The VOF multiphase model was selected to compute the phase volume fractions of the two phases, namely the slag and atmosphere. Species transport of the dissolving refractory component into the slag was implemented using the 2nd order discretization scheme. The refractory was modeled as a rigid wall, with a mass fraction of the dissolving refractory component set equal to its saturation limit within the slag at the given temperature.

The simulations were conducted utilizing the commercial code ANSYS Fluent 2022 R2, Version 22.2.0. The pressure-based solver and the SIMPLE pressure-velocity coupling scheme were employed. The flow was assumed to be laminar, and the 2nd order momentum discretization scheme was used. The ANSYS Fluent methods are detailed in Ansys Inc [37]. The VOF compressive scheme was used to ensure accurate interface depiction [56,57].

2.4.1. *Suitability of the simulation model and settings*

2.4.1.1. Boundary condition for the section model. The appropriateness of the cut section was evaluated by simulating alumina at 1550 °C, assuming a constant surface tension. A no-slip boundary condition and a symmetry boundary were considered as suitable choices for the bottom of the section model. Both conditions were applied in this study, and the outcomes were compared. Fig. 3 illustrates the wall shear stress profile along the refractory/slag interface and the species mass fraction along the slag/atmosphere interface for a specific time step for the models with different boundary conditions. Similar simulation results were obtained with any of the chosen boundary condition at the domain

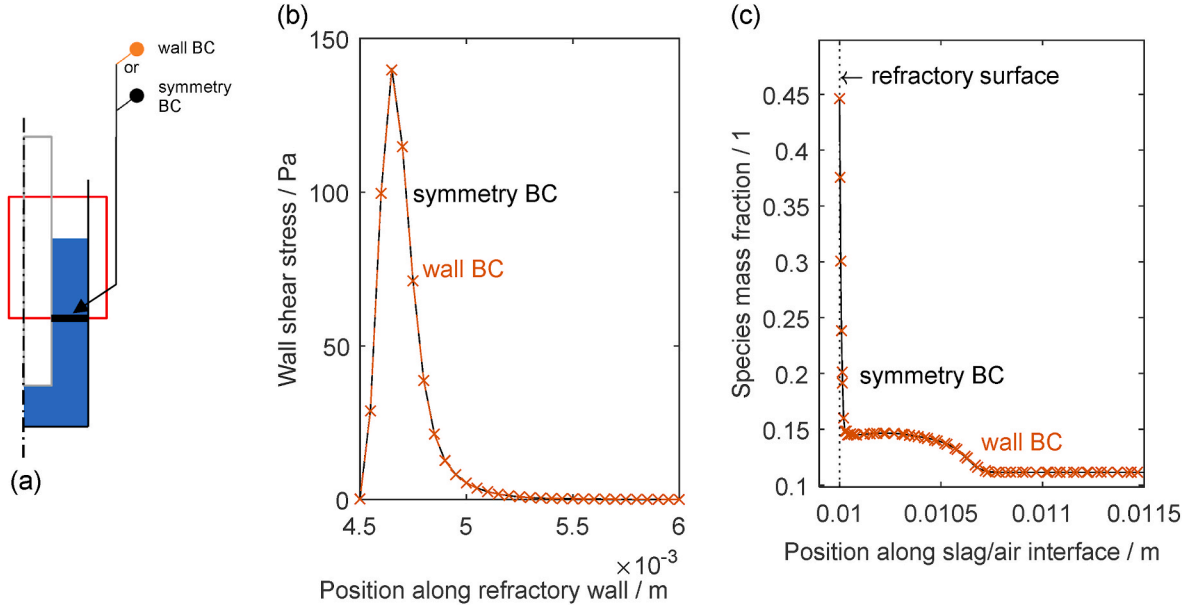

Fig. 3. Schematic of the modeled section (a), wall shear stress along the refractory wall with slag contact (b) and species mass fraction along the slag/air interface (c) obtained by modelling with the wall (red) and symmetry (black) boundary conditions. (For interpretation of the references to colour in this figure legend, the reader is referred to the Web version of this article.)

bottom.

2.4.1.2. Choice of the multiphase and surface tension model. The VOF multiphase model was verified against the Eulerian model. For the VOF model, implicit and explicit methods for solving the governing equations were applied and compared. Meanwhile, for the Eulerian model, the explicit method was used. Two surface tension models, namely the continuous surface force (CSF) and continuous surface stress (CSS) models, are available in Fluent for modeling surface tension forces. Although the VOF explicit method is expected to perform best in suppressing numerical diffusion and maintaining the sharpness of the interface, no difference was observed when the implicit method was used. Thus, the simulations were calculated using the implicit VOF model, which has a lower cost. Fig. 4 illustrates the clear relationship of the resultant slag/atmosphere interfaces (VOF = 0.95) between the Eulerian CSF, VOF CSF, and VOF CSS models in the simulation of alumina in the CASM slag at 1550 °C with variable surface tension. Furthermore, the simulated ascension height of 4.9 mm aligns closely with the analytical results of 4.1 mm, calculated according to Langbein [58] for wetting a flat surface.

The derivative of the mass fraction of the dissolving species with respect to the distance in the direction normal to the refractory wall is plotted with respect to time in Fig. 5. The area-weighted average of species mass fraction derivatives over two different sections is plotted. No discernible differences are observed between the CSF and CSS surface-tension models. Consequently, the simulations were conducted using the CSS model, which yielded more stable results compared to the CSF model. Additionally, the values obtained correspond well with the Eulerian model.

2.4.1.3. Mesh resolution. The grid along the slag/atmosphere interface was further refined by halving the cell dimensions up to 155 466 cells. Subsequently, the simulation results with the original and refined mesh were compared. Fig. 6 depicts the average derivative of the species mass fraction along the refractory wall from the initial bath level to the end of the domain and from the triple point to the end of domain with respect to time for the current and refined meshes. The simulation results of the refined mesh closely match those of the original mesh, with a maximum relative error of 1.4 %. Consequently, further calculations were conducted using the original mesh without additional refinement.

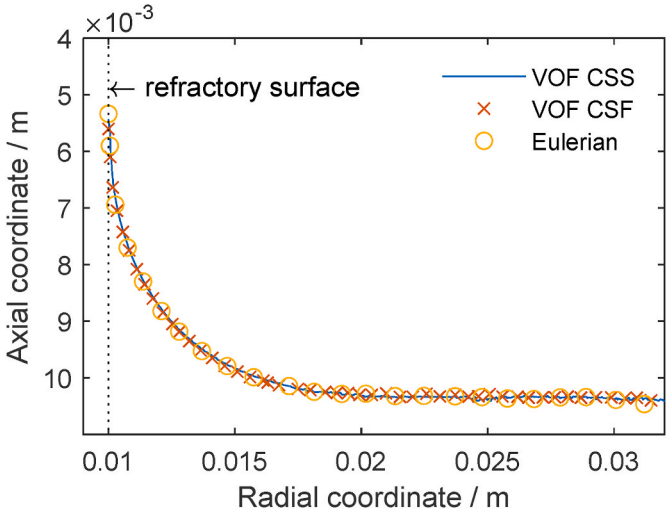

Fig. 4. Contour plots of the Eulerian CSF, VOF CSF, and VOF CSS models at the slag/air interface for 4.5 s.

3. Results

3.1. Experimental results

Figs. 7–9 illustrate the magnesia and alumina samples after the corrosion test in the CASM slag at 1550 and 1500 °C and their corresponding wear profiles for each step. In all cases, a discernible local corrosion zone is evident. Specifically, for alumina corroded at 1550 and 1500 °C, the average groove radius exhibits a decrease at a mean rate across the corrosion steps of 0.39 and 0.15 mm/h, respectively. Meanwhile, the decrease in the groove radius for magnesia at 1500 °C is 1.10 mm/h. The groove heights and average groove radii after each step for the three experiments are detailed in Table 3.

3.2. Results of the analytical consideration

The corrosion rates were calculated according to Eq. (12) using the mass-transfer coefficients determined using Eq. (4) [19], yielding a more accurate slag film thickness and groove length, including the Stefan flow effect. The corrosion rates were determined using Eqs. (13) and (14) [17] and are summarized in Table 4. The densities and surface tension of the slag at the initial conditions were employed in the calculation. A wetting angle of 30° was assumed. The densities of 3208.3 and 3727.3 kg/m^3 were employed for magnesia and alumina, respectively. The recorded groove height was determined following the final corrosion step, and the average corrosion rate was derived from the experimental data.

Significant deviation was noted across all cases, yet reliable predictions were confirmed specifically for magnesia using the adapted equation. Since the formulated equations were derived for slag films, favorable predictions were anticipated when applying them to the region above the slag bath level. The ascension height determined according to Langbein [58] was used to obtain the groove height and groove length calculated from the measurement data within the region. The results are denoted as v_2' and presented in Table 6. The results demonstrated an enhanced prediction of the corrosion rate for alumina at 1550 °C solely, achieving a relative error of 8 %.

The experimental measurement data enables the calculation of corrosion rates through the utilization of mass transfer coefficients specific to each corrosion step. The total mass-transfer coefficients based on the equation of Pötschke [19] were obtained using the more accurate slag film thickness and groove length by applying the slag densities and surface tension for the solute content at the middle of the step. Hence, predictions for groove radii can be made for each corrosion step. The subsequent comparison between the predicted and measured average groove radii is illustrated in Fig. 10. In the case of magnesia, the computed groove radii align with the measured values, with exceptions noted in the initial two steps. Conversely, for alumina, a notable variance is evident, and the reduction in groove radii was consistently underestimated at 1500 °C and during the final two steps at 1550 °C.

3.3. Simulation results

Simulations were performed on a computer with an Intel(R) Core (TM) i7-3930K processor running with four parallel nodes. Simulation for a flow time of 60 s required the operation time of 13 days.

Figs. 11 and 12 illustrate the mass fraction derivatives and wall shear stresses with respect to the position along the refractory wall for the magnesia/CASM slag at 1500 °C and alumina/CASM slag at 1550 °C, respectively. Additionally, contour plots of the species mass fraction with the velocity vector in the near-wall section of the simulation model were generated. The developed Marangoni flow recirculation is evident in the contour plots for both alumina and magnesia, extending in the same direction, towards the refractory wall at the free surface. However, the recirculation developed to a larger extent for magnesia. The profile marked by the mass fraction derivative in Fig. 11 depicts a groove

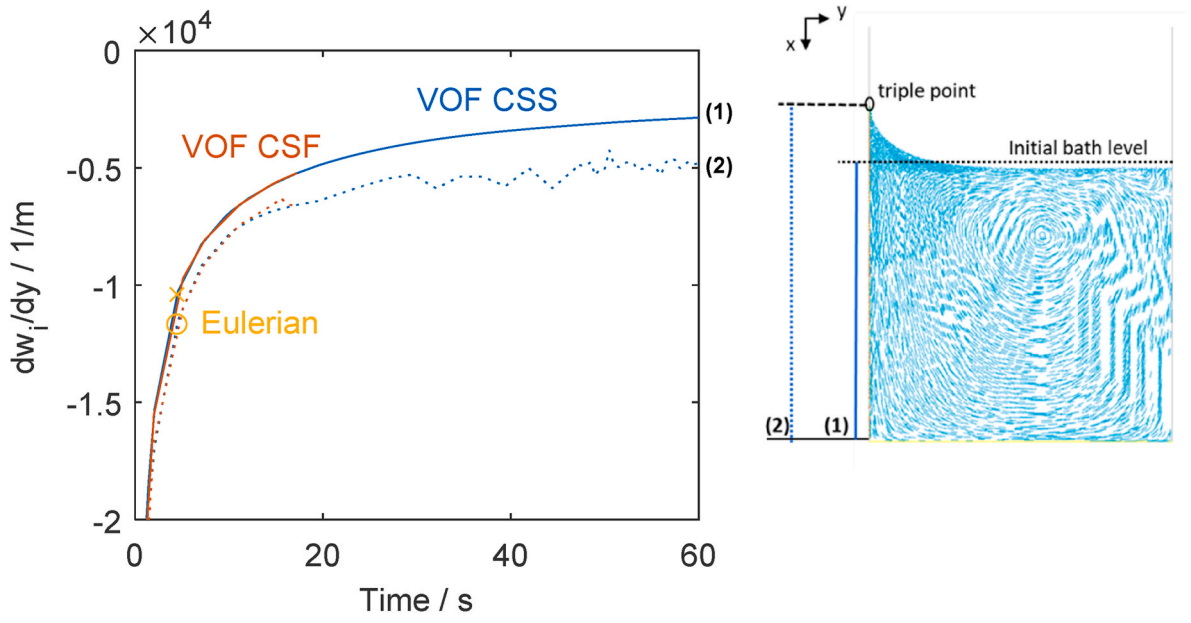

Fig. 5. Average derivative of the species mass fraction along the refractory wall from the initial bath level to the end of the domain (1) and along the refractory wall in slag contact (2) with respect to time for the VOF CSF and VOF CSS models and for one time step of the Eulerian CSF model.

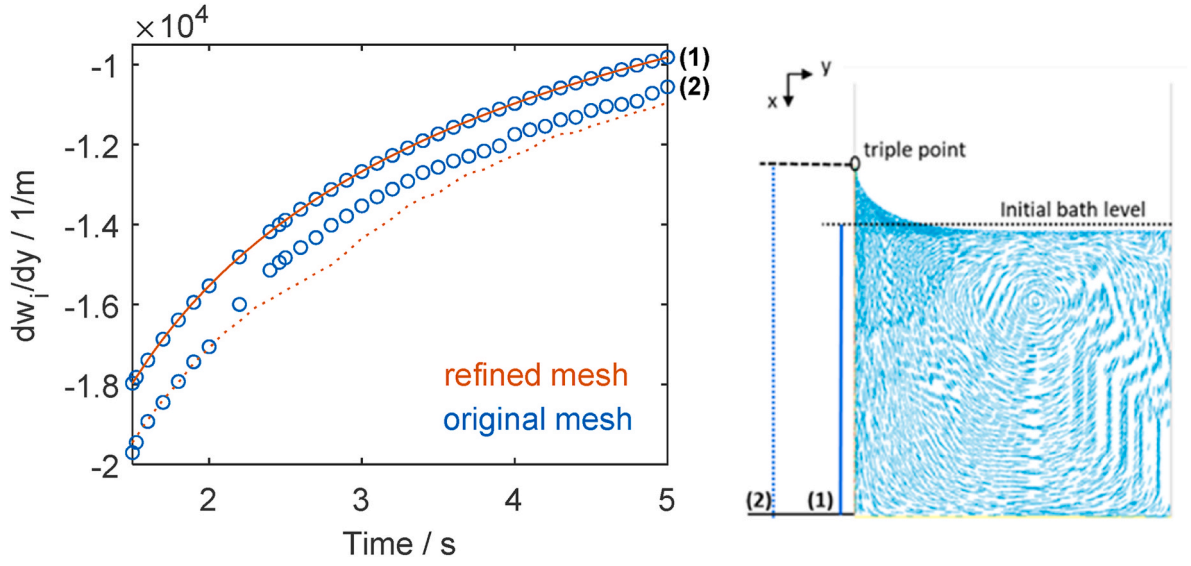

Fig. 6. Average derivative of the species mass fraction with time along the refractory wall from the initial bath level to the end of the domain (1) and from the triple point to the end of the domain (2) for the current (blue) and refined (orange) meshes. (For interpretation of the references to colour in this figure legend, the reader is referred to the Web version of this article.)

formation.

Fig. 13(a) illustrates the mass fraction derivative along the refractory wall for different time steps. The absolute local minima in the wall shear-stress profile, signifying the position where two counter-directed recirculation zones intersect, were identified to define the groove section Fig. 13(a). The initially high scatter levels out at later times. Meanwhile, the range of variable mass-fraction derivatives associated with the groove formation increased with time. The local absolute maxima in the mass fraction derivative were used to fix the groove section for each time step. The local maxima were determined within certain ranges and indicated by the yellow lines in the diagram in Fig. 11(a). Fig. 13(b) illustrates the exemplary section representing the groove for several time steps. For alumina, the smaller recirculation zone extends more into the upper thin slag film. The scattering in the profiles of the mass-transfer derivative in this upper droplet-shaped recirculation zone is higher, which hinders the tracking of the upper border of the groove section. The absolute local minima in the wall shear-stress profile, signifying the position where two counter-directed recirculation zones intersect, were identified to define the groove section.

For the groove sections, an average Sherwood number *Sh* was calculated using Eq. (15):

$$Sh = \left|\frac{dw_i}{dy}\right| \cdot \frac{L}{w_{i,s} - w_{i,0}}, \tag{15}$$

where dw_i/dy is the mass fraction derivative, L is the annular gap between the refractory finger and crucible, and $w_{i,s}$ and $w_{i,0}$ are the saturated and initial mass fraction of the dissolving species, respectively. Fig. 14 illustrates the average *Sh* on the groove with respect to time.

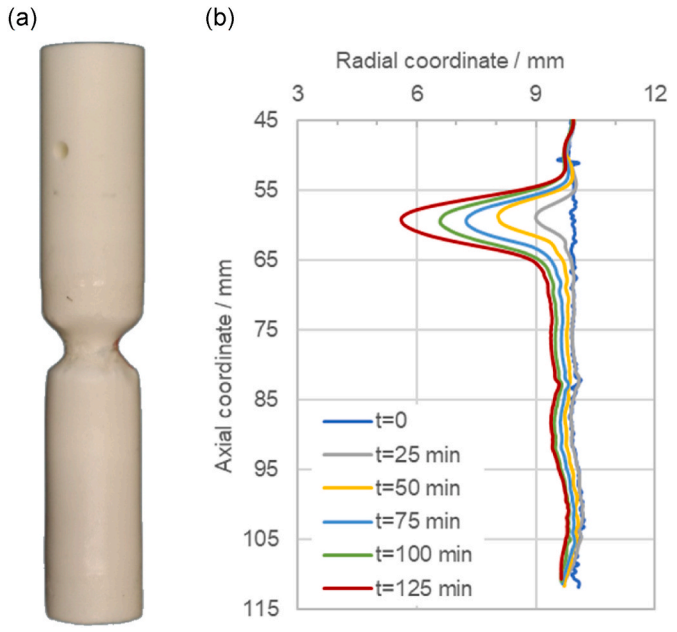

Fig. 7. Photograph of the magnesia sample after the static corrosion test of CASM slag at 1500 °C for 125 min (a) and corresponding wear profiles for the corrosion steps (b).

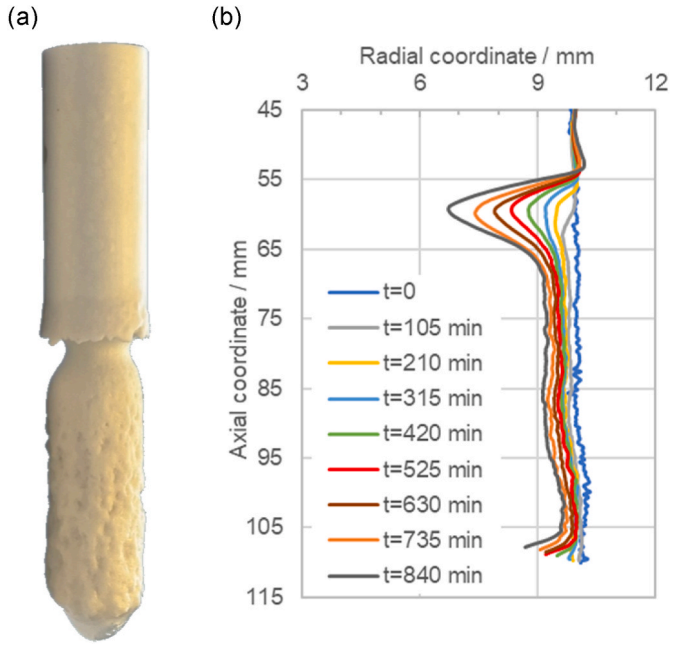

Fig. 8. Photograph of the alumina sample after the static corrosion test of the CASM slag at 1500 °C for 840 min (a) and the corresponding wear profiles for the corrosion steps (b).

Curve fitting was applied to extrapolate *Sh* to the experimental time, thereby overcoming the time-scale problems. Nonlinear least-square method was used to determine the parameters for an exponential function of

$$Sh = a \cdot \left(1 - b \cdot \exp\left(c \cdot t^{d}\right)\right), \tag{17}$$

where *a* is in the range of 0–200. Using the correlation *Sh* as a function of time, the mean sample radius in the groove section can be predicted by integration as follows:

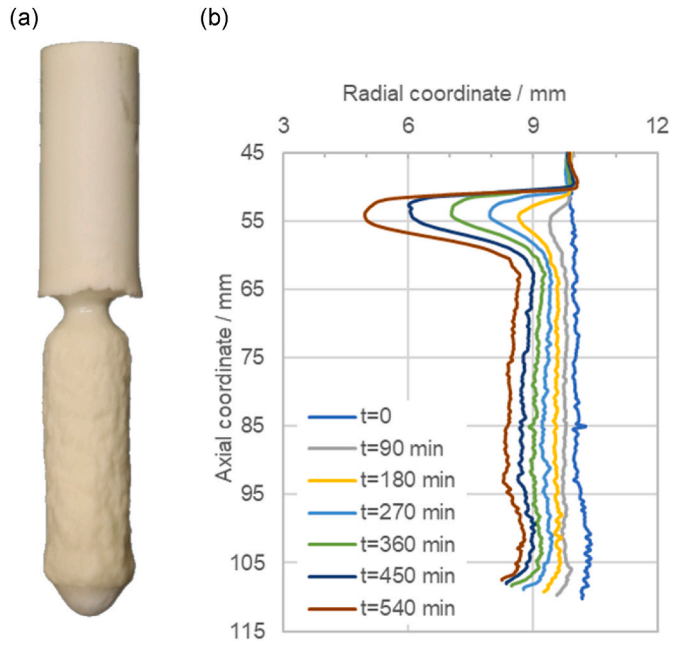

Fig. 9. Photograph of the alumina sample before and after the static corrosion test of the CASM slag at 1550 °C for 540 min (a) and the corresponding wear profiles for the corrosion steps (b).

Table 3
Groove height (h) and average groove radius (r) after each corrosion step for magnesia at 1500 °C and alumina at 1500 and 1550 °C in the CASM slag.

Step	M/CASM at 1500 °C		A/CASM 1500 at °C		A/CASM 1550 at °C	
	h/mm	r/mm	h/mm	r/mm	h/mm	r/mm
1	7.19	9.88	4.26	9.71	7.38	9.54
2	10.01	8.93	7.82	9.57	8.42	9.08
3	13.11	8.53	9.13	9.36	8.94	8.56
4	13.60	8.14	10.31	9.14	10.19	8.01
5	13.77	7.73	10.52	8.85	10.72	7.31
6			11.48	8.60	10.42	6.46
7			12.68	8.31		
8			12.80	7.91		

Table 4
Results of the analytical considerations.

	M/CASM 1500 °C	A/CASM 1500 °C	A/CASM 1550 °C
v_1/mm/h	0.607	0.065	0.208
v_2/mm/h	1.062	0.108	0.241
v_2'/mm/h	3.074	0.326	0.426
v_{Hrma}/mm/h	1.17–2.35	0.203–0.405	0.388–0.776
v_{Exp}/mm/h	1.096	0.150	0.395
Rel. error v_1 to v_{Exp}	−45 %	−56 %	−47 %
Rel. error v_2 to v_{Exp}	−3 %	−28 %	−39 %

$$R_t = R_0 - \chi \cdot \frac{w_{i,s} - w_{i,0}}{1 - w_{i,s}} \cdot \frac{\rho}{\rho_r} \cdot \frac{D}{L} \cdot \int_0^{t_f} Sh(t)dt \tag{18}$$

The R_t values in the groove based on the simulation results are listed in Table 5 to Table 7, where parameters a, b, c, and d for Eq. (17) are also provided. The measured groove radii for the corrosion steps of the experiments are listed, including the relative error between the predicted and measured radii.

Table 5
Predicted mean and measured groove radii for the corrosion steps of magnesia in the CASM slag at 1500 °C.

Step	Time/ min	Measured mean sample radius in the groove/ mm	Predicted mean sample radius in the groove[a]/ mm	Relative error
		10.00		
1	25	9.882	9.785	0.98 %
2	50	8.928	9.667	8.27 %
3	75	8.528	8.713	2.17 %
4	100	8.145	8.313	2.06 %
5	125	7.726	7.930	2.64 %

[a] Deduced from $Sh = a \cdot (1 - b \cdot \exp(c \cdot t^d))$, where $a = 5.613$, $b = 2.81 \times 10^{-4}$, $c = 13.42$, and $d = -0.04128$.

Table 6
Predicted mean and measured groove radii for the corrosion steps of alumina in the CASM slag at 1550 °C.

Step	Time/ min	Measured mean sample radius in the groove/ mm	Predicted mean sample radius in the groove[a]/ mm	Relative error
		10.01		
1	90	9.534	8.206	14.02 %
2	180	9.069	7.741	14.74 %
3	270	8.553	7.275	15.04 %
4	360	7.997	6.759	15.58 %
5	450	7.297	6.203	15.12 %
6	540	6.446	5.504	14.76 %

[a] Deduced from $Sh = a \cdot (1 - b \cdot \exp(c \cdot t^d))$, where $a = 10.35$, $b = -27.67$, $c = 2.479$, and $d = -0.4605$.

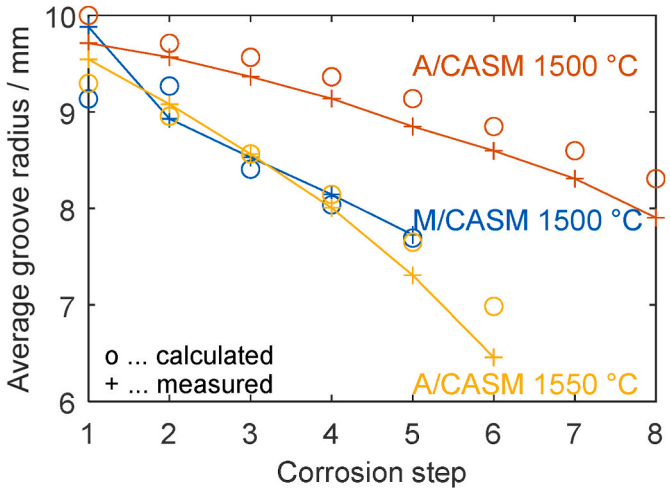

Fig. 10. Calculated and measured average groove radii for magnesia at 1500 °C (blue) and alumina at 1500 °C (red) and 1550 °C (yellow). (For interpretation of the references to colour in this figure legend, the reader is referred to the Web version of this article.)

4. Discussion

4.1. Experimental results

The experimental results demonstrate the highest dissolution rate for magnesia, leading to the implementation of short corrosion steps to prevent sample breakage due to rapid neck formation. Conversely, for alumina at a higher temperature (1550 °C), an elevated dissolution rate is observed. The time derivatives of the radius decreased, and the *Sh* values suggest a steadier dissolution, as given in Fig. 15. Similar behavior at 1500 °C and 1550 °C is observed even when the viscosity was reduced to approximately 73 % at the higher temperature. For magnesia, the trends in the first and second steps deviate from the observed steady state evident in the last three steps. The wear profiles of magnesia revealed the absence of corrosion along the mantle surface after the first corrosion step (Fig. 7). This suggests the likelihood of phase formation, potentially a spinel formation, occurring after the initial corrosion step during the dropping time before measurement. This formed phase was subsequently easily dissolved in the second corrosion step, potentially explaining the higher dissolution rate observed in the second step. While additional phase formation is anticipated during the dropping time, its impact on the measurement vanishes. Phase formation during dropping time is also expected for alumina (FactSage calculations reveal CMA_{12} and CM_2A_{27}). Due to the extended corrosion steps, specifically 105 and 90 min for alumina at 1500 and 1550 °C, respectively, in contrast to 25 min for magnesia, phase formation might have minimal effects on the measurements. This is because the reaction layer may rapidly dissolve within the subsequent corrosion step. In addition, for the alumina cases, the radius decreased along the mantle after the first step indicating minor phase formation.

The mantle surface of alumina exhibits a rough texture at both temperatures. The cause of this phenomenon remains unknown and lies beyond the scope of the current study. A smooth surface for the same systems was observed from rotating finger tests [52], suggesting the flow instabilities that vanished under forced convection. Additional investigation is necessary to elucidate the mechanisms behind the observed surface roughness. Nevertheless, the impact of these mechanisms on the groove cannot be disregarded.

4.2. Analytical results

The modifications made to the Pötschke equation, as presented, resulted in an enhancement over the original equations. Analytical calculations align with the observation of corrosion rate values, indicating magnesia > alumina at 1550 °C > 1500 °C. Notably, for alumina, the predicted corrosion rates exhibit similar magnitudes for both temperatures, consistent with experimental findings. This reaffirms the presence of a dissolution process controlled by species diffusion in the liquid as the predominant wear mechanism. However, the equation tends to underestimate the corrosion rate for alumina, except for the initial two steps at 1500 °C. However, a satisfactory fit to measurements was achieved for the magnesia/CASM system. The prediction of the analytical groove radii was inaccurate for the first two steps and corresponded well for the later steps derived by the dissolution equation, as depicted in Fig. 10. This confirms the influence of phase formation on the dissolution of magnesia, thereby affecting the measurement. However, substituting the ascension height in the equation, rather than the groove height, led to a decline in estimation accuracy. Specifically, a satisfactory alignment with measurements was only attained for alumina at 1550 °C in the later steps.

4.3. Simulation results

The current simulation model effectively portrayed the Marangoni flow. The velocities at the atmosphere/slag interphase are directed towards the refractory wall, where the surface tension forces are largest. Here, the concentration of the dissolving species reaches the highest value corresponding to saturation, which translates to the higher surface tension values shown in Table 1. As a result of this, a recirculation flow is induced, posing the typical pattern of the Marangoni flow. Locally concentration gradients of the dissolving species are steeper. As a consequence, the dissolution mass flux is increased, local corrosion is observable. From counter plots of the species mass fractions given in Figs. 11 and 12 the effect of the flow field on the species distribution is visible. The species boundary layer at the refractory wall is thinned at

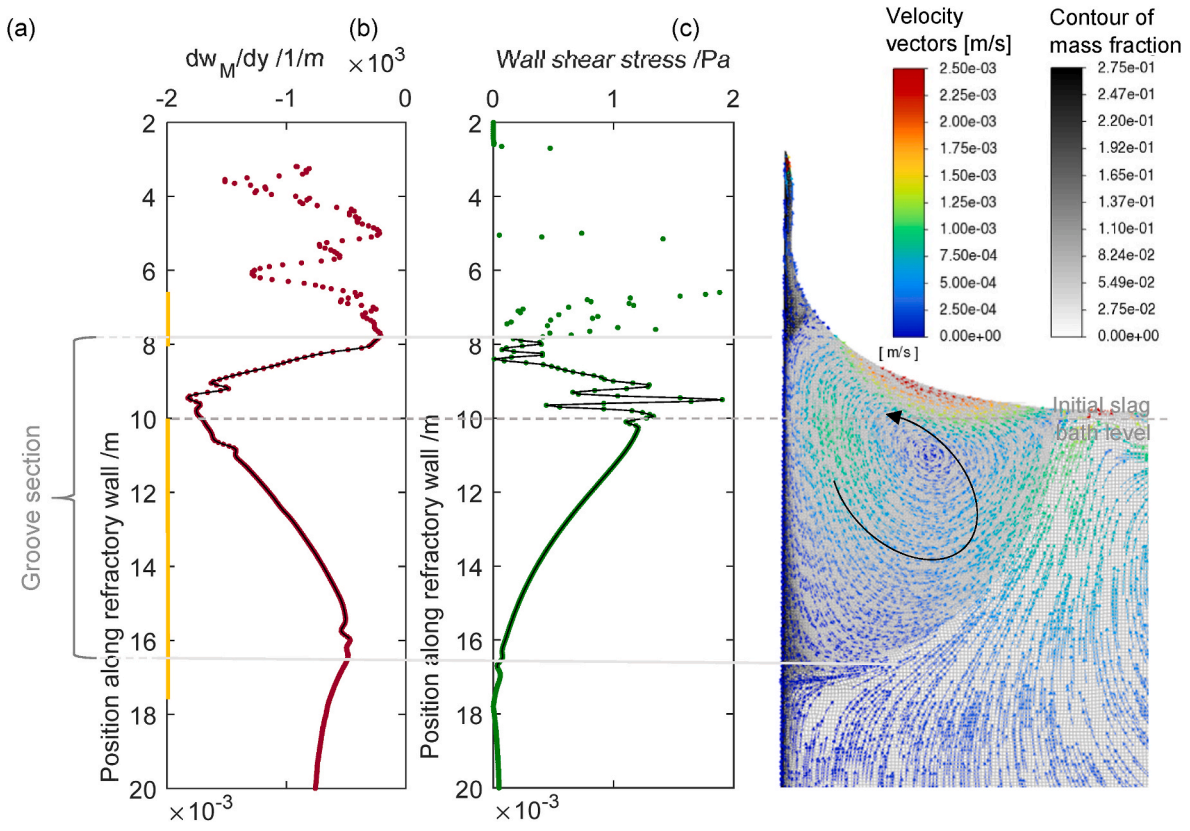

Fig. 11. Mass fraction derivative (a) and shear stress (b) with respect to the position along the refractory wall for magnesia at 1500 °C and 99.5 s. Contour plot of the magnesia mass fraction with the velocity vectors near the wall of the simulation model (c).

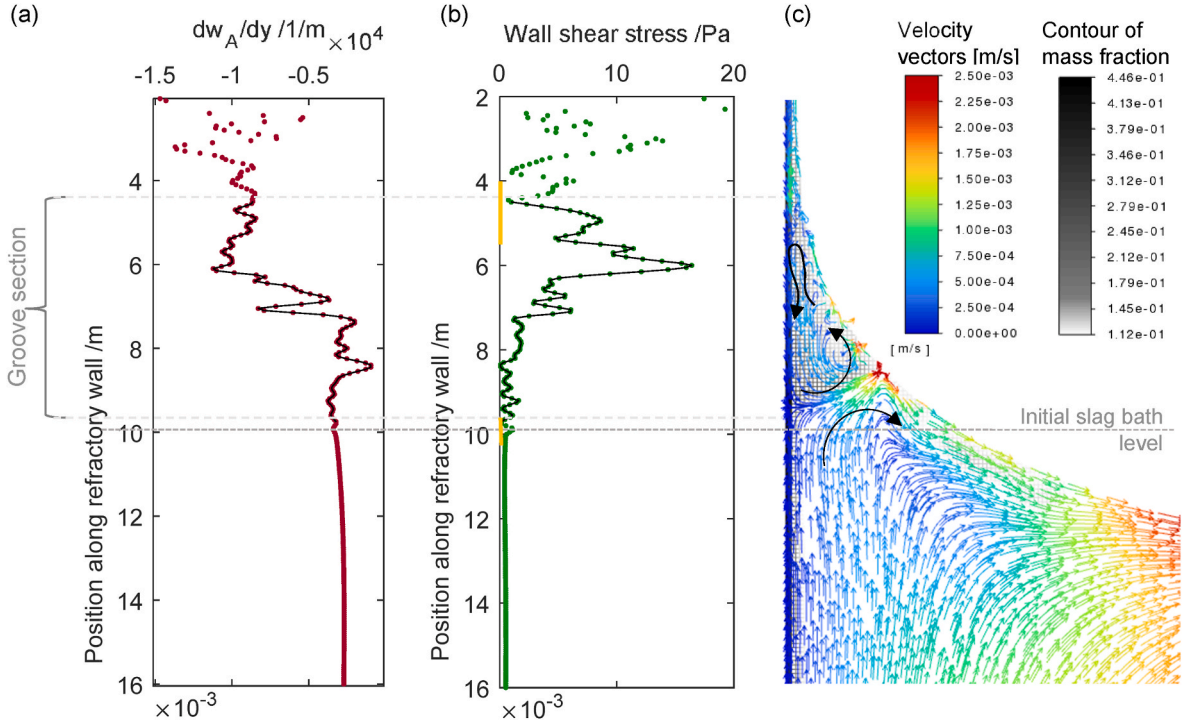

Fig. 12. Mass fraction derivative (a) and wall shear stresses (b) with respect to the position along the refractory wall for alumina at 1550 °C at 70.75 s. Contour plots of the alumina mass fraction with the velocity vectors near the wall of the simulation model.

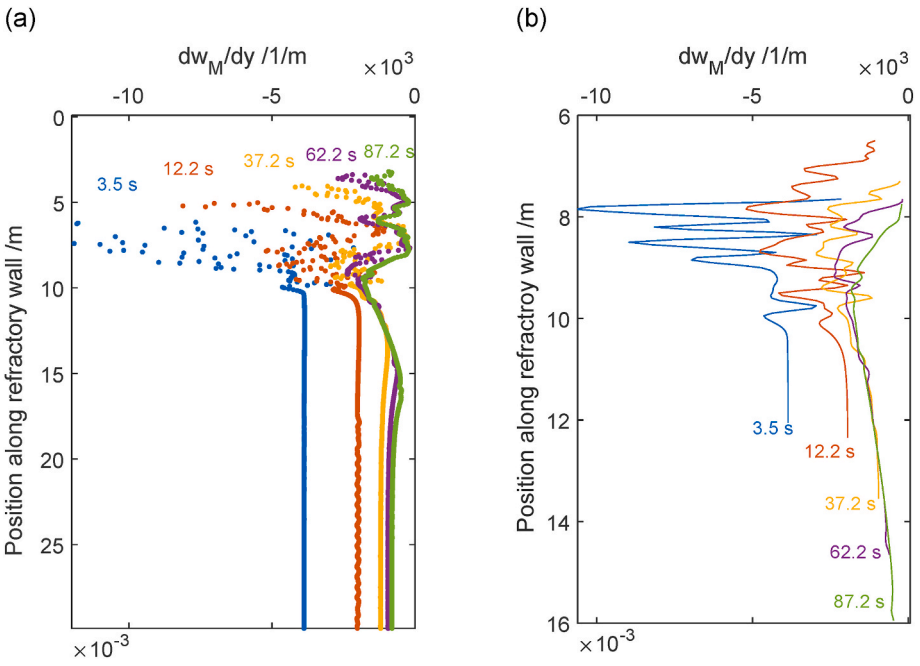

Fig. 13. Mass fraction derivative with respect to the position along the refractory wall for different time steps (a) and for sections representing the groove of magnesia at 1500 °C (b).

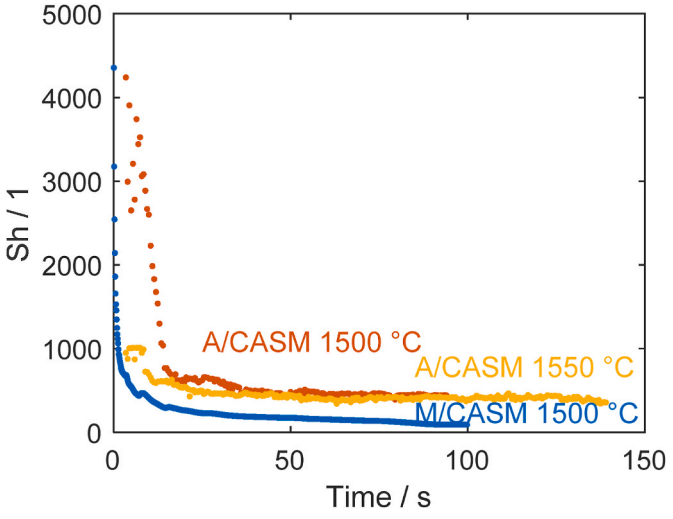

Fig. 14. Simulated *Sh* in the groove section with time.

the high axial velocity region of the Marangoni vortices. The profiles of the mass fraction derivatives plotted in Figs. 11 and 12 clearly show this influence of the Marangoni flow, derivatives decrease where the recirculation zone of Marangoni flow is located. Thus, species diffusion and as a consequence corrosion is locally accelerated.

The use of multiphase and surface-tension models proved suitable in this study, showing no significant discrepancies when compared to alternative models. The results noted the negligible effects of the mesh resolution.

The application of the section model to depict the Marangoni flow in the groove is justified because the extent of Marangoni recirculation flow remains well within the domain. The bottom boundary of the domain is approximately 1.5 times the recirculation zone for magnesia and significantly larger at 3.3 times the recirculation zone for alumina. However, it's noteworthy that the saturation of the slag bath evolved more rapidly within the model of the entire assembly, impacting mass transfer and diminishing precision.

Table 7
Predicted mean and measured groove radii for the corrosion steps of alumina in the CASM slag at 1500 °C.

Step	Time/ min	Measured mean sample radius in the groove/ mm	Predicted mean sample radius in the groove[a]/ mm	Relative error
		10.010		
1	105	9.712	8.724	10.17 %
2	210	9.566	8.425	11.93 %
3	315	9.364	8.280	11.58 %
4	420	9.138	8.078	11.60 %
5	525	8.849	7.852	11.27 %
6	630	8.598	7.563	12.04 %
7	735	8.308	7.311	12.00 %
8	840	7.905	7.022	11.17 %

[a] Deduced from $Sh = a \cdot (1 - b \cdot \exp(c \cdot t^d))$, where $a = 122.813$, $b = -1.922$, $c = 7.9837$, and $d = -0.7547$.

Fig. 16 depicts the measured groove heights of each corrosion step for magnesia at 1500 °C and alumina at 1500 and 1550 °C. The groove height enlarges and stabilizes as the corrosion progresses, suggesting the increase of the advancing corrosion groove depth. A consistent groove height is attained at the conclusion of the experiment for magnesia and alumina at 1500 °C, and just before the final step for alumina at 1550 °C. In Fig. 16 the simulated average height of the groove section is plotted. Despite a notable difference in simulated and experimental times, the mean heights of the assessed sections obtained through simulation align well with the observed trend in the evolution of measured groove height. Thus, the simulated and evaluated sections, as described in Section 3.3, fixed by the local extrema in the mass fraction derivatives and wall shear stresses, respectively, can properly represent the groove height.

An increased scatter of species derivatives in the groove area, particularly noticeable for alumina, poses challenges in the simulation, especially initially. This can be attributed to lower diffusion coefficients. However, the scatter diminishes at later stages of the experiments, enhancing results for alumina. The wall shear stresses in the alumina groove are about one order of magnitude higher than those in magnesia,

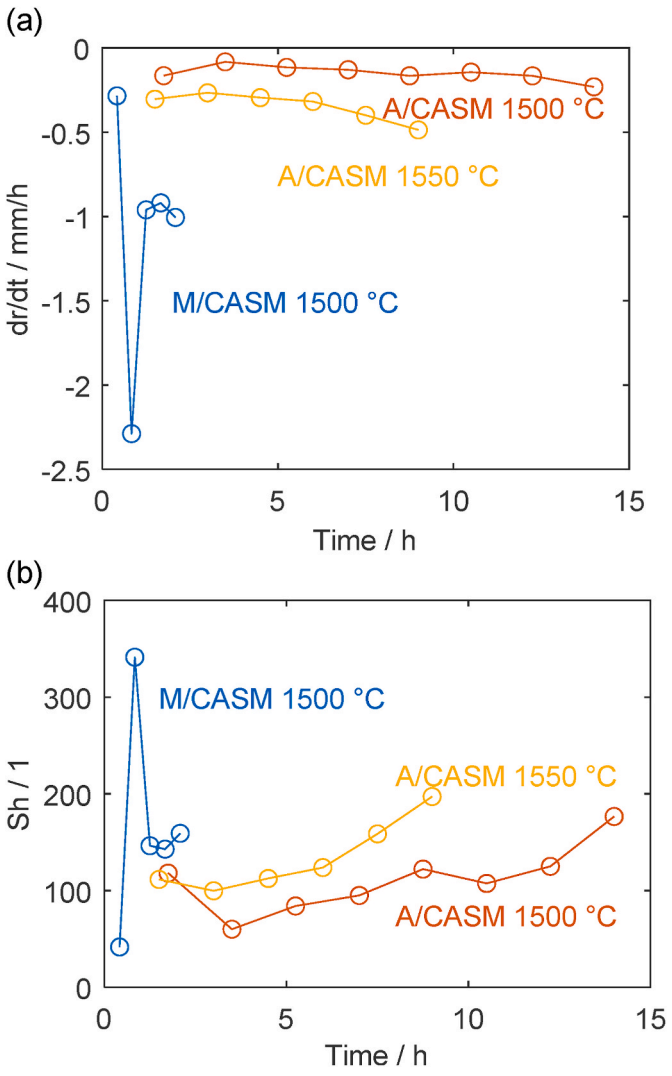

Fig. 15. Time derivative of the measured radius (a) and *Sh* (b).

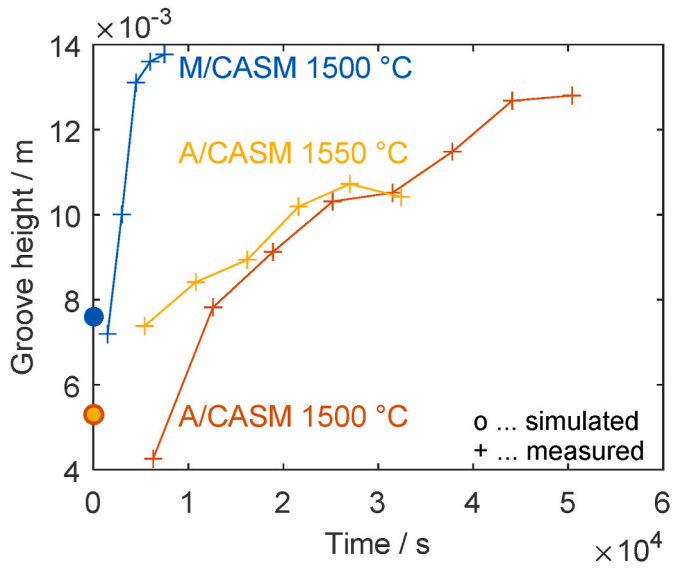

Fig. 16. Groove height obtained by measurement and simulation of the estimated groove section for magnesia at 1500 °C (blue) and alumina at 1500 °C (red) and 1550 °C (yellow). (For interpretation of the references to colour in this figure legend, the reader is referred to the Web version of this article.)

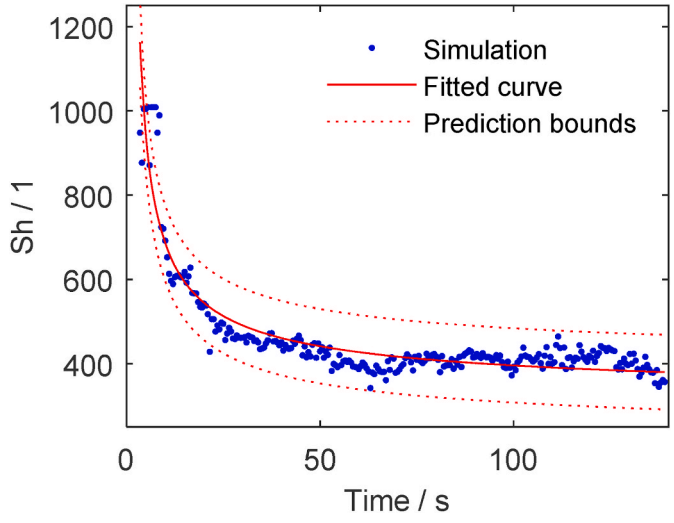

Fig. 17. *Sh* of A/CASM at 1550 °C obtained by simulation and the fitting curve with 95 % confidence.

potentially promoting erosion. Despite this, the highest wear rate is observed for magnesia, restricting the contribution of erosion to total wear. Additionally, the dissolution models successfully describe the wear rate, reinforcing this conclusion.

The 95 % confidence prediction bounds and fitting curves are provided in Fig. 17. Despite the shorter simulated times compared to the experimental duration, which imposes limitations on reliability, extrapolation enabled the prediction of groove radii up to the experimental time scale. Notably, for the alumina case at 1550 °C, the highest uncertainty was observed. At 5400 s, corresponding to the 1st corrosion step, a broad interval of 159–463 was obtained for the predicted *Sh* of 310. For magnesia, the error in the predicted radius based on the *Sh* extrapolation by curve fitting is approximately 2 % for the later steps. The first step could be predicted accurately, whereas only a higher error was noted for the 2nd step. The deviations of the trends for the second step were also noted in the analytical methods. This aligns with the hypothesis of phase formation influence. However, the extrapolation for alumina produced less accurate estimates due to increased scatter in simulation results. This discrepancy suggests that seemingly negligible effects might significantly contribute to total wear. The unidentified phenomena influencing surface roughness on worn alumina samples may impact wear within the groove, contributing to larger discrepancies between simulation and experimental values, as these mechanisms were not incorporated into the model.

The simulation assumed constant slag density and viscosity values, overlooking the potential impact of solute dependencies on these properties during dissolution, including density-driven flow effects. In actual application, a saturated slag is in direct contact with the refractory, and the slag properties of the slag bulk change depending on the solute content during dissolution. The density of the magnesia-saturated slag increases by approximately 5.4 % [48], whereas viscosity decreases by approximately 71 %, according to FactSage calculations. In alumina systems, viscosity rises with alumina addition. Calculations based on FactSage indicate that the viscosity of alumina-saturated slag increases by approximately 228 % and 195 % of its initial value at 1500 and 1550 °C, respectively. This phenomenon can account for the more significant disparities observed between simulation and experimental values for the alumina systems. Additionally, density values of alumina-saturated slag increase by 3.3 % and 3.6 % at 1500 and 1550 °C, respectively.

For magnesia at 1500 °C, the increase in the magnesia content by approximately 1.5 wt% increased the density by 0.4 % and decreased in

Table 8
Time scales for the different systems.

		M/CASM at 1500 °C	A/CASM at 1500 °C	A/CASM at 1550 °C
Diffusion time scale	$T_D = L^2/2D$	9.85×10^5	5.95×10^6	3.40×10^6
Viscous time scale	$T_\mu = L^2/(\mu/\rho)$	1.80	1.80	2.47
Advection time scale[a]	$T_A = L_R/v_{a,\max}$	26.3	18.4	18.8

[a] From the simulation for one specific time step.

the viscosity by approximately 13.6 % after 125 min. For the alumina dissolution at 1550 °C, the increase in the alumina content by approximately 3.1 wt% after 540 min of dissolution increased the slag viscosity by 14.8 %. Meanwhile, at a corrosion time of 840 min and a temperature of 1500 °C, an observed increase in alumina content by 1.9 wt% led to a 9.4 % rise in viscosity. The simulations assumed constant effective binary diffusivities. The decline in viscosity during magnesia dissolution can enhance the diffusive mass flux due to an increased diffusion coefficient. Conversely, a reduction in the diffusion coefficient is anticipated to decrease the mass flux during alumina dissolution. In the dissolution process, the refractory can be considered a semipermeable surface, permitting the dissolution of certain species while hindering the entry of other slag species. This entails an equalizing flow perpendicular to the refractory/slag interface directed into the bulk slag, that is, a Stefan flow, which was not considered in the simulation. Thus, its effect on the species distribution and consequently, on the surface tension was not modeled. In a post-processing step, its effect was accounted for using Eq. (9), where $\chi/(1-w_s)$ is 1.188 for the magnesia/CASM system and 1.317 and 1.346 for the alumina/CASM system at 1500 and 1550 °C, respectively. Nevertheless, its influence during dissolution is missing, indicating several discrepancies.

Table 8 lists the diffusion and viscous time sales calculated with L as the gap width. The ratio of the maximal axial velocity near the refractory surface $v_{A,max}$ to the initial wetted length of the refractory surface L_R, as determined from the simulation at a specific time step (115 s), can serve as the advection time scale. The viscous and advection time scales exhibit similarity, while the diffusion time scale for alumina at the same temperature is approximately six times larger. This suggests that quasisteady behavior is achieved after a longer duration for the alumina system compared to the magnesia system. This discrepancy could account for the enhanced results observed for magnesia.

This study validated the existence of a diffusion-controlled dissolution process, highlighting the Marangoni flow as the key factor in the localized corrosion of magnesia. Simulations provided these results, further supported by the adapted analytical equation. The findings constrain the influence of wear from erosion caused by wall shear stresses and buoyancy flow or flow instabilities due to viscosity gradients. Thus far, investigations reported in literature could not assert that with this certainty. However, the density and viscosity flows appear to remarkably increase alumina wear. This conclusion is drawn from both simulations and analytical considerations, corroborated by the observed sample roughness post-experiments. The potential influence of density and viscosity flows may be explored in future studies.

5. Conclusion

In this study, the local corrosion of magnesia and alumina in a CASM slag at 1500 and 1550 °C was investigated by experimental, analytical, and computational methods. Analytical corrosion rates for the alumina systems exhibited discrepancies compared to measured dissolution rates, with the analytical equation underestimating the measurements. Utilizing precise measurement data from the CWTD improved the accuracy of values. In contrast, for magnesia, analytical results aligned well with measurement values, affirming the suitability of applied equations in providing accurate data. This finding strengthens the understanding of wear as primarily driven by diffusion-controlled dissolution without significant erosion. The higher deviation for alumina suggests the involvement of additional phenomena, beyond the Marangoni effect, in the dissolution process, a notion supported by the rough surface of worn alumina samples.

The CFD modeling of a segment of the finger-test assembly effectively identified the Marangoni flow and its impact on corrosive mass transfer. Extrapolating simulation results facilitated predicting groove radii on measurement time scales. A more substantial disparity between predicted and measured groove radii was observed in the alumina system. This can be attributed partly to the investigation method, notably the longer diffusion time scale of alumina compared to magnesia, necessitating extended simulation times for quasi-steady behavior and introducing heightened uncertainties. Additionally, inaccuracies were heightened in the alumina system due to unconsidered effects such as the concentration dependency of slag properties and Stefan flow, surpassing those in the magnesia system. Conversely, the higher deviation in the alumina system may suggest that diverse phenomena, beyond the Marangoni flow, contributed to corrosion. The latter interpretation aligns with analytical findings and is further substantiated by the visibly rougher mantle surface of the alumina samples. This study contributes to the understanding of wear mechanisms in the absence of forced convection, quantifying local wear. Future research will extend beyond the influence of the Marangoni flow to explore additional phenomena, including convection driven by density and viscosity gradients, to comprehensively examine their impact on local corrosion.

Funding

The authors gratefully acknowledge the funding support from the K1-MET GmbH, metallurgical competence center. The research program of the K1-MET competence center is supported by COMET (Competence Center for Excellent Technologies), the Austrian program for competence centers. COMET is funded by the Federal Ministry for Climate Action, Environment, Energy, Mobility, Innovation and Technology, the Federal Ministry for Digital and Economic Affairs, the Federal States of Upper Austria, Tyrol, and Styria as well as the Styrian Business Promotion Agency (SFG) and the Standortagentur Tyrol. Furthermore, we thank Upper Austrian Research GmbH for the continuous support. In addition to the public funding from COMET, this research project is partially financed by the scientific partners the Chair of Ceramics of the Montanuniversität Leoben, and the industrial partners, namely voestalpine Stahl GmbH, RHI Magnesita GmbH, and Böhler Edelstahl GmbH.

Data statement

The data used in this study are provided in the text and its Supporting Information.

CRediT authorship contribution statement

Sandra Vollmann: Writing – review & editing, Writing – original draft, Visualization, Software, Methodology, Investigation, Formal analysis, Conceptualization. **Jerónimo Guarco:** Writing – review & editing, Visualization, Methodology, Conceptualization. **Burhanuddin:** Writing – review & editing, Investigation.

Declaration of competing interest

The authors declare no conflicts of interest.

Acknowledgment

The authors thank Prof. H. Harmuth for supervision and for

providing the resources.

References

[1] Y. Chen, G.A. Brooks, S.A. Nightingale, Slag line dissolution of MgO refractory, Can. Metall. Q. 44 (2005) 323–330, https://doi.org/10.1179/cmq.2005.44.3.323.
[2] Z.F. Yuan, W.L. Huang, K. Mukai, Local corrosion of magnesia-chrome refractories driven by Marangoni convection at the slag-metal interface, J. Colloid Interface Sci. 253 (2002) 211–216, https://doi.org/10.1006/jcis.2002.8504.
[3] H. Harmuth, V. Kircher, N. Kölbl, Main wear mechanisms of SEN slag band materials, China's Refractories (2017) 1–7.
[4] S. Seetharaman (Ed.), Treatise on Process Metallurgy: Volume 2: Process Phenomena, Elsevier, 2014.
[5] J. Pötschke, T. Deinet, The corrosion of AMC-refractories by steel and slag, in: Proceedings of the Unified International Technical Conference on Refractories, Orlando, Florida, USA, 2005, pp. 75–79.
[6] J. Pötschke, R. Simmat, Corrosion of dense refractories by glass melts or slags, in: Proceedings of the Unified International Technical Conference on Refractories, Orlando, Florida, USA, 2005, pp. 695–698.
[7] K. Mukai, T. Masuda, K. Gouda, T. Harada, J. Yoshitomi, S. Fujimoto, Local corrosion of solid oxides at the liquid (PbO-SiO_2) slag-Pb interface, J.Japan Inst. Metals 48 (1984) 726–734, https://doi.org/10.2320/jinstmet1952.48.7_726.
[8] K. Mukai, T. Harada, T. Nakano, K. Hiragushi, Mechanism of local corrosion of solid silica at PbO-SiO_2 slag surface, J.Japan Inst.Metals 50 (1986) 63–71, https://doi.org/10.2320/jinstmet1952.50.1_63.
[9] K. Mukai, J.M. Toguri, J. Yoshitomi, Corrosion of alumina–graphite refractories at the slag–metal interface, Can. Metall. Q. 25 (1986) 265–275, https://doi.org/10.1179/cmq.1986.25.4.265.
[10] Z. Yu, K. Mukai, K. Kawasaki, I. Furusato, Relation between corrosion rate of magnesia refractories by molten slag and penetration rate of slag into refractories, J. Ceram. Soc. Japan 101 (1993) 533–539, https://doi.org/10.2109/jcersj.101.533.
[11] Z. Yu, K. Mukai, Direct observation of the local corrosion of solid silica at the surface of liquid Fe_tO-SiO_2 slags, J.Japan Inst.Metals 56 (1992) 1137–1144, https://doi.org/10.2320/jinstmet1952.56.10_1137.
[12] K.T. Mukai, Z.L. Matsushita, Direct observation of interfacial phenomena, such as local corrosion, slag and metal penetration into refractories, using a high temperature X-ray radiographic technique, in: Proceedings of the 10th International Ceramics Congress, Florence, Italy, Techna, Faenza, Italy, 2003, pp. 23–34.
[13] Z.F. Yuan, S. Xie, X. Yu, Y. Zhang, R. Wang, Local corrosion mechanism of SiO2-based refractories caused by slag movement near solid–liquid–gas interface in different slag systems, Trans. Nonferrous Metals Soc. China 29 (2019) 1975–1982, https://doi.org/10.1016/S1003-6326(19)65105-8.
[14] M.Z. Tao, K. Mukai, Local corrosion of magnesia-chrome refractory at slag-metal interface, Taikabutsu Overseas 19 (1999) 3–10.
[15] P. Lian, A. Huang, H. Gu, Y. Zou, L. Fu, Y. Wang, Towards prediction of local corrosion on alumina refractories driven by Marangoni convection, Ceram. Int. (2018) 1675–1680, https://doi.org/10.1016/j.ceramint.2017.10.095.
[16] V. Stanek, J. Szekely, The effect of surface driven flows on the dissolution of a partially immersed solid in a liquid-analysis, Chem. Eng. Sci. 25 (1970) 699–715, https://doi.org/10.1016/0009-2509(70)85099-0.
[17] P. Hrma, Dissolution of a solid body governed by surface free convection, Chem. Eng. Sci. 25 (1970) 1688, https://doi.org/10.1016/0009-2509(70)80059-8.
[18] B. Han, C. Ke, Y. Wei, W. Yan, C. Wang, F. Chen, N. Li, Degradation of MgO–C refractories corroded by SiO2–Fe2O3–V2O5–TiO2–MnO–MgO slag, Ceram. Int. 41 (2015) 10966–10973, https://doi.org/10.1016/j.ceramint.2015.05.040.
[19] J. Pötschke, C. Bürggmann, Permature wear of refractories due to marangoni-convection, Steel Res. Int. 83 (2012).
[20] K. Fagerlund, S. Sun, S. Jahanshahi, Effect of Marangoni-induced flow on the rate of refractory dissolution in molten slags, Scand Jof Metallurgy 31 (2002) 359–366, https://doi.org/10.1034/j.1600-0692.2002.00542.x.
[21] Burhanuddin, H. Harmuth, S. Vollmann, Determining the critical Reynolds number for suppressing Marangoni convection of alumina in silicate melt, Ceram. Int. 50 (2024) 18323–18328, https://doi.org/10.1016/j.ceramint.2024.02.316.
[22] M.I.H. Siddiqui, L. Arifudin, I.A. Alnaser, M.A. Ali, K. Alluhydan, Modeling of interfacial tension and inclusion motion behavior in steelmaking continuous casting mold, Materials 16 (2023), https://doi.org/10.3390/ma16030968.
[23] C. Wecker, A. Schulz, J. Heine, H.-J. Bart, E.Y. Kenig, Droplet formation – a numerical investigation of liquid-liquid systems with consideration of Marangoni convection, Int. J. Heat Mass Tran. 188 (2022) 122465, https://doi.org/10.1016/j.ijheatmasstransfer.2021.122465.
[24] Q.-J. Yang, Q. Mao, W. Cao, Numerical simulation of the Marangoni flow on mass transfer from single droplet with different Reynolds numbers, Colloids Surf. A Physicochem. Eng. Asp. 639 (2022) 128385, https://doi.org/10.1016/j.colsurfa.2022.128385.
[25] M. Moezzi, M. Sajjadi, S.H. Hejazi, Thermally driven Marangoni effects on the spreading dynamics of droplets, Int. J. Multiphas. Flow 159 (2023) 104335, https://doi.org/10.1016/j.ijmultiphaseflow.2022.104335.
[26] A. Javadi, M. Karbaschi, D. Bastani, J.K. Ferri, I. Kovalchuk, N.M. Kovalchuk, K. Javadi, R. Miller, Marangoni instabilities for convective mobile interfaces during drop exchange: experimental study and CFD simulation, Colloids Surf. A Physicochem. Eng. Asp. 441 (2014) 846–854, https://doi.org/10.1016/j.colsurfa.2012.10.032.
[27] R.F. Engberg, M. Wegener, E.Y. Kenig, The impact of Marangoni convection on fluid dynamics and mass transfer at deformable single rising droplets – a numerical study, Chem. Eng. Sci. 116 (2014) 208–222, https://doi.org/10.1016/j.ces.2014.04.023.
[28] Y.-H. Siao, C.-D. Wen, Examination of molten pool with Marangoni flow and evaporation effect by simulation and experiment in selective laser melting, Int. Commun. Heat Mass Tran. 125 (2021) 105325, https://doi.org/10.1016/j.icheatmasstransfer.2021.105325.
[29] A. Caboussat, J. Hess, A. Masserey, M. Picasso, Numerical simulation of temperature-driven free surface flows, with application to laser melting and polishing, J. Comput. Phys. X 17 (2023) 100127, https://doi.org/10.1016/j.jcpx.2023.100127.
[30] D.-W. Cho, Y.-D. Park, M. Cheepu, Numerical simulation of slag movement from Marangoni flow for GMAW with computational fluid dynamics, Int. Commun. Heat Mass Tran. 125 (2021) 105243, https://doi.org/10.1016/j.icheatmasstransfer.2021.105243.
[31] J. Ou, A. Chatterjee, S.L. Cockcroft, D.M. Maijer, C. Reilly, L. Yao, Study of melting mechanism of a solid material in a liquid, Int. J. Heat Mass Tran. 80 (2015) 386–397, https://doi.org/10.1016/j.ijheatmasstransfer.2014.09.022.
[32] I. Seric, S. Afkhami, L. Kondic, Direct numerical simulation of variable surface tension flows using a Volume-of-Fluid method, J. Comput. Phys. 352 (2018) 615–636, https://doi.org/10.1016/j.jcp.2017.10.008.
[33] B. Zhang, B. Boyd, Y. Ling, Direct numerical simulation of compressible interfacial multiphase flows using a mass–momentum–energy consistent volume-of-fluid method, Comput. Fluid 236 (2022) 105267, https://doi.org/10.1016/j.compfluid.2021.105267.
[34] G. Mialhe, S. Tanguy, L. Tranier, E.-R. Popescu, D. Legendre, An extended model for the direct numerical simulation of droplet evaporation. Influence of the Marangoni convection on Leidenfrost droplet, J. Comput. Phys. 491 (2023) 112366, https://doi.org/10.1016/j.jcp.2023.112366.
[35] P. Horgue, M. Prat, M. Quintard, A penalization technique applied to the "Volume-Of-Fluid" method: wettability condition on immersed boundaries, Comput. Fluid 100 (2014) 255–266, https://doi.org/10.1016/j.compfluid.2014.05.027.
[36] F. Denner, B.G. van Wachem, Compressive VOF method with skewness correction to capture sharp interfaces on arbitrary meshes, J. Comput. Phys. 279 (2014) 127–144, https://doi.org/10.1016/j.jcp.2014.09.002.
[37] Ansys, Inc, Fluent user and theory guide, Fluent Release 2020 R1, https://ansyshelp.ansys.com, 2023. (Accessed 27 July 2023).
[38] Ansys, Inc., Ansys fluent multiphase flow modeling lecture volume of fluid model. https://fliphtml5.com/pexb/golm/basic, 2023. (Accessed 27 July 2023).
[39] F. Denner, F. Evrard, B.G. van Wachem, Breaching the capillary time-step constraint using a coupled VOF method with implicit surface tension, J. Comput. Phys. 459 (2022) 111128, https://doi.org/10.1016/j.jcp.2022.111128.
[40] F. Denner, B.G. van Wachem, Numerical time-step restrictions as a result of capillary waves, J. Comput. Phys. 285 (2015) 24–40, https://doi.org/10.1016/j.jcp.2015.01.021.
[41] C. Galusinski, P. Vigneaux, On stability condition for bifluid flows with surface tension: application to microfluidics, J. Comput. Phys. 227 (2008) 6140–6164, https://doi.org/10.1016/j.jcp.2008.02.023.
[42] J.U. Brackbill, D.B. Kothe, C. Zemach, A continuum method for modeling surface tension, J. Comput. Phys. 100 (1992) 354, https://doi.org/10.1016/0021-9991(92)90240-Y.
[43] S. Vollmann, H. Harmuth, Marangoni convection as a contribution to refractory corrosion - CFD simulation and analytical approaches, in: Proceedings of the Unified International Technical Conference on Refractories, Victoria, BC, United States, John Wiley & Sons, USA, 2014, pp. 857–862.
[44] J. Guarco, Burhanuddin, S. Vollmann, H. Harmuth, Sherwood correlation for finger-test experiments, Results in Engineering 15 (2022) 100610, https://doi.org/10.1016/j.rineng.2022.100610.
[45] J. Guarco, S. Vollmann, H. Harmuth, Burhanuddin, Method for inverse calculation of erosion parameters in slag-refractory systems, Mater. Today Commun. 33 (2022) 104736, https://doi.org/10.1016/j.mtcomm.2022.104736.
[46] Q. Wang, C. Tan, C. Liu, Z. Chen, W. Yan, G. Li, Elaboration of A Coupled numerical model for predicting magnesia refractory damage behavior in high-temperature reactor, Metall. Mater. Trans. B (2023), https://doi.org/10.1007/s11663-023-02947-6.
[47] Q. Wang, C. Liu, L. Pan, Z. He, G. Li, Numerical understanding on refractory flow-induced erosion and reaction-induced corrosion patterns in ladle refining process, Metall. Mater. Trans. B 53 (2022) 1617–1630, https://doi.org/10.1007/s11663-022-02471-z.
[48] J. Xin, L. Gan, L. Jiao, C. Lai, Accurate density calculation for molten slags in SiO2–Al2O3–CaO–MgO systems, ISIJ Int. 57 (2017) 1349, https://doi.org/10.2355/isijinternational.ISIJINT-2017-070.
[49] H. Harmuth, Burhanuddin, Evaluation of CLSM measurements for dissolution studies – a case study investigating alumina dissolution in a silicate slag, Ceram. Int. 48 (2022) 28180, https://doi.org/10.1016/j.ceramint.2022.06.120.
[50] H. Harmuth Burhanuddin, Dissolution of magnesia in silicate melts and diffusivity determination from CLSM studies, Appl. Sci. 13 (2023) 8458, https://doi.org/10.3390/app13148458.
[51] H. Harmuth Burhanuddin, S. Vollmann, Quantification of magnesia dissolution in silicate melts and diffusivity determination using rotating finger test, Appl. Sci. 12 (2022) 12791, https://doi.org/10.3390/app122412791.
[52] J. Guarco Burhanuddin, H. Harmuth, S. Vollmann, Application of an improved testing device for the study of alumina dissolution in silicate slag, J. Eur. Ceram. Soc. 42 (2022) 3652–3659, https://doi.org/10.1016/j.jeurceramsoc.2022.02.056.

[53] J. Guarco, Burhanuddin, S. Vollmann, H. Harmuth, Method for determination of effective binary diffusivities in dissolution of dense ceramic materials, Ceram. Int. 48 (2022) 7456–7463, https://doi.org/10.1016/j.ceramint.2021.11.264.

[54] J. Xin, N. Wang, M. Chen, L. Gan, Surface tension calculation of molten slag in SiO2–Al2O3–CaO–MgO systems based on a statistical modelling approach, ISIJ Int. 59 (2019) 767, https://doi.org/10.2355/isijinternational.ISIJINT-2018-746.

[55] V. Kircher, Burhanuddin, H. Harmuth, Design, operation and evaluation of an improved refractory wear testing technique, Measurement 178 (2021) 109429, https://doi.org/10.1016/j.measurement.2021.109429.

[56] F. Denner, D.R. van der Heul, G.T. Oud, M.M. Villar, A. Da Silveira Neto, B.G. van Wachem, Comparative study of mass-conserving interface capturing frameworks for two-phase flows with surface tension, Int. J. Multiphas. Flow 61 (2014) 37–47, https://doi.org/10.1016/j.ijmultiphaseflow.2013.12.011.

[57] V.R. Gopala, B.G. van Wachem, Volume of fluid methods for immiscible-fluid and free-surface flows, Chem. Eng. J. 141 (2008) 204–221, https://doi.org/10.1016/j.cej.2007.12.035.

[58] D.W. Langbein, Capillary surfaces shape - stability - dynamics, in: Particular under Weightlessness, Springer, Berlin, 2002.